Journal of Radiation Research and Applied Sciences 18 (2025) 101830

Contents lists available at ScienceDirect

Journal of Radiation Research and Applied Sciences

journal homepage: www.journals.elsevier.com/journal-of-radiation-research-and-applied-sciences

Structural and defects analysis of electron irradiated low-cost biochar for dosimetry application

Umme Muslima [a,*], Mayeen Uddin Khandaker [a,b,c,**], S.N. Mat Nawi [a], Md Raghib Rahat [a], S.E. Lam [a], H.J. Woo [d], N.M. Ung [e], Nora Almuqbil [f], Zuhal Y. Hamd [f], Chien Ing Yeo [g]

[a] Applied Physics and Radiation Technologies Group, CCDCU, Faculty of Engineering and Technology, Sunway University, Bandar Sunway, 47500, Selangor, Malaysia
[b] Department of Physics, College of Science, Korea University, 145 Anam-ro, Seongbuk-gu, Seoul, 02841, Republic of Korea
[c] Faculty of Graduate Studies, Daffodil International University, Daffodil Smart City, Birulia, Savar, Dhaka, 1216, Bangladesh
[d] Centre for Ionics Universiti Malaya, Department of Physics, Faculty of Science, Universiti Malaya, 50603, Kuala Lumpur, Malaysia
[e] Clinical Oncology Unit, Faculty of Medicine, University of Malaya, 50603, Kuala Lumpur, Malaysia
[f] Department of Radiological Sciences, College of Health and Rehabilitation Sciences, Princess Nourah bint Abdulrahman University, P.O. Box 84428, Riyadh 11671, Saudi Arabia
[g] Sunway Biofunctional Molecules Discovery Centre, School of Medical and Life Sciences, Sunway University, Bandar Sunway, 47500, Selangor, Malaysia

ARTICLE INFO

Keywords:
Coconut shell biochar
Electron irradiation
Raman spectroscopy
Photoluminescence (PL) spectra
Scanning electron microscopy (SEM)
X-ray diffraction (XRD)

ABSTRACT

This work evaluates the appropriateness of electron irradiated low-cost biochar for passive radiation dosimetry by focusing on the structural alteration within the doses between 2 and 20 Gy. Scanning Electron Microscopy (SEM) has been employed to investigate the morphological changes of the biochar. SEM images revealed microstructural damage and increased porosity with higher doses. Raman spectroscopy, Photoluminescence (PL) spectroscopy and X-ray diffraction (XRD) have been performed to investigate the correlation between absorbed energy of radiation and associated material modifications. These spectroscopies provide insight into the physical characteristics associated with the imperfections and contributing to the luminescence process. The intensity ratio, I_D/I_G from raman spectra and the deconvoluted peak areas varies with doses and is related to the degree of domination of defect production and defect annealing. The crystallite size is inversely proportional to I_D/I_G ratio. PL spectroscopy also confirmed the structural modification of biochar with radiation doses and the large band gap determined from the PL spectra of biochar is to be 4.63 ± 0.01 eV, confirms the ability to store charge for long term. By analyzing lattice strain (ε), crystallite size (D), dislocation density (δ) and full width at half maximum (FWHM) from X-ray diffraction (XRD) patterns, additional evidence of structural changes within the investigated range of dose was obtained. Overall, SEM, Raman spectroscopy, PL and XRD confirm the dose dependent structural change of biochar for electron irradiation. These structural study research findings reveal that biochar offers a number of favorable advantages for radiation dosimetry. Its potential as a sustainable, affordable, and adaptive substitute for traditional inorganic dosimetric materials is highlighted by its carbon-rich structure, sensitivity to defect evolution, and structural stability under electron irradiation. All these results point to its potential in prospective radiation sensing applications.

1. Introduction

Carbonaceous materials such as charcoal, graphite, and black carbon have long been used as writing and drawing tools. Since carbonaceous materials have lower density, outstanding thermal and electrical conductivity, better corrosion resistance, capability of reinforcement, their application has been found recently in a wide range of fields, including electronics, sensors, composite materials, energy storage and conversion, medical applications, and so on (Khan et al., 2014).

Charcoal-based applications have numerous medical uses, including as a drug nanocarrier, acute poisoning neutralizer and antidot for drug overdose, and less commonly, treating the skin infections, malodorous

* Corresponding author.
** Corresponding author. Applied Physics and Radiation Technologies Group, CCDCU, Faculty of Engineering and Technology, Sunway University, Bandar Sunway, 47500, Selangor, Malaysia.
E-mail addresses: ummemuslima15@gmail.com (U. Muslima), mayeenk@sunway.edu.my (M.U. Khandaker).

https://doi.org/10.1016/j.jrras.2025.101830
Received 18 May 2025; Received in revised form 3 July 2025; Accepted 23 July 2025
Available online 28 July 2025

wound and irritation related to dialysis (Brooks et al., 2017). The process of pyrolyzing organic matter, such as agricultural waste, in an oxygen-limited atmosphere results in biochar, a form of carbon rich substance. Biochar is beneficial in many applications owing to its diverse range of attributes. The structure of biochar is usually highly porous, offering it an enormous amount of surface area. It is evident from Lam et al. (2023) that the substance with large surface area exhibits the greatest thermoluminescence (TL) behavior. In recent years, the feasibility of employing carbon-based materials for radiation dosimetry has been thoroughly investigated to demonstrate their efficiency. Nawi et al. (2021) conducted an investigation into pencil lead graphite (PPLG) concerning electron irradiation, emphasizing structural analysis and determining trapping parameters from glow curve. The findings indicate that PPLG offers significant potential in both diagnostic and therapeutic dosimetry applications with a limitation of their fragility and inconsistent carbon content. Lam et al. (2021) investigated human hair with raman and PL spectroscopy under gamma irradiation and recommended further comprehensive research to support those hairs might facilitate swift medical triage, with proper dose estimation. By employing raman spectroscopy and photoluminescence (PL), Bradley et al. (2022) studied the radiation-induced defects in pencil rod of various diameters and graphite sheet for cobalt-60 gamma, 6 MeV electron, photon from x-ray machine and thermal neutron. Certain forms of charcoal, such as mangrove, coconut, and sawdust also provided potential platform in radiation dosimetry for gamma ray dose range of 0–10 Gy (Almugren et al., 2022). Lam et al. (2023) investigated graphite sheet of different thicknesses and activated carbon as a radiotherapy dosimeter using well-positioned imperfection-dependent analytical procedure including thermoluminescence (TL), photoluminescence (PL), and raman micro-spectroscopy at low linear energy with gamma irradiation and found a certain limitation regarding density for application. Later, Muslima et al. (2025); Muslima et al. (2024) investigated the TL response of biochar for cobalt 60 gamma and Linac photon and confirmed its suitability for dosimetric application.

Motivated by the previous studies on carbonaceous material and their potential TL features, we were prompted to investigate biochar under electron irradiation as a medium for TL dosimetry. Additionally, recent investigations on TL properties for biochar have been limited to cobalt-60 gamma and Linac photon irradiation, with no systematic study assessing its response to electron beam. Biochar samples are easily accessible and can be employed as the basis for both dosimetric probe and low-cost, high-performing sample for researching radiation-induced alterations in carbonaceous composites. The skin dose can be measured favorably because the effective atomic number (Z_{eff}) of biochar is comparable to soft tissue of human (Muslima et al., 2025). Coconut shell biochar has gained increasing attention as a sustainable and versatile material due to its superior physicochemical properties. Its high carbon content, low ash, and uniform microporous structure make it particularly suitable for a range of applications, including thermoluminescence (TL) dosimetry (Ighalo et al., 2023; Ajien et al., 2023). Moreover, the production of coconut shell biochar through processes such as pyrolysis and gasification yield a carbon-rich material with high porosity and large surface area, both of which are beneficial for efficient charge trapping in TL-based systems (Ajien et al., 2023). These attributes, combined with its abundant availability, cost-effectiveness, and environmental sustainability, make coconut shell biochar a promising and practical candidate over other carbonaceous materials such as mangrove or sawdust for radiation dosimetry applications. To bridge the research gap obtained from literature, the current work aims to determine the structural modifications of biochar along with the features of defects engaged in the luminescence process under electron irradiation ranges between 0 and 20 Gy. The study used state-of-the-art technologies for characterizing carbonaceous biochar, namely scanning electron microscopy (SEM), Raman spectroscopy, Photoluminescence spectroscopy (PL) and x-ray diffraction (XRD). It is anticipated that the outcomes of this study will lead to conclude biochar as a cost-effective material to monitor electron dose that may be utilized as passive radiation dosimeters in medical application.

2. Materials and method

2.1. Preparation and irradiation of sample

For this study, we employed biochar made from coconut shells that was bought from a Malaysian commercial source. Following sample collection, the sample was taken to the lab and crushed with a pestle and mortar to produce fine particles. The fine powder samples were sieved along with a micrometer mesh to produce a consistent grain size. The samples underwent exposure to an electron beam using a LINAC at the Oncology department of the University Malaya Medical Center (UMMC). Electron irradiation was carried out at a dose rate of 600 MU/min. To ensure reproducibility, measurements were made in triplicate ($n = 3$) for each dose level. For every set, the mean and standard deviation were reported. For irradiation, full-scatter conditions were obtained by positioning the biochar samples at the center of a 10×10 cm^2 field using a solid-waterTM phantom. Samples were covered with 1.5 cm-thick tissue-equivalent bolus material, to attain the maximum doses. Furthermore, an established source to surface distance (SSD) of 100 cm was maintained. To ascertain the structural alterations, the samples underwent exposure to radiation with a dose range from 2 Gy to 20 Gy with 6 MeV electron.

2.2. Characterization of sample

2.2.1. Morphological analysis

Secondary electron imaging is a technique used in scanning electron microscopy (SEM) to examine the morphology and surface topology of materials at the micron and nanoscale (Li et al., 2021). Surface morphological radiation damage was detected using SEM imaging for the electron exposure from linac accelerator at doses ranging between 2 Gy and 20 Gy for 100 μm scale bar. The Tescan VEGA3, which was employed in this investigation, is a high-performance analytical SEM with an acceleration voltage of 30 kV that can operate in both low- and high-vacuum modes.

2.2.2. Raman spectroscopy and photoluminescence (PL) measurement

Confocal Raman spectroscopy (alpha300 RA, WITec GmbH, Germany) situated at Sunway University was utilized to examine radiation-driven structural modifications and imperfections in the samples at room temperature. To stimulate the samples, a green laser light with an energy of 2.33 eV and a numerical aperture of 0.9 was used, along with an objective lens of 100 × . The dispersed signal from Raman was identified using an optic multi-fibre pointed toward a spectrometer utilizing an optical grating of 600 g mm^{-1}. A CCD camera then captured the signal for 10 s. In order to eliminate cosmic ray noise, which causes sharp spikes in Raman spectra, the raw spectrum data was processed using the WITec Project FIVE 5.3 software. Raman spectra were obtained from several random points on the surface of each sample to account for local differences and make the data more reliable. The obtained spectra are the average of three measurements made at different places for each dose condition. This technique confirms that structural changes were always present and that localized surface anomalies had the least effect. Three samples were examined to get the Raman measurements, and from these data the ratio from the average intensity value of the graphite (G) and defect (D) peaks was calculated, which is known as I_D/I_G. The peak area of the D and G bands was analyzed using OriginPro 2018's Peak Analyzer software to get the I_D/I_G ratio. The Tuinstra-Koenig equation (Tuinstra & Koenig, 1970) was used to calculate the in-plane crystallite size L_a of the biochar sample.

$$L_{a(nm)} = \left(2.4 \times 10^{-10}\right)\lambda_{laser}^{4}\left(\frac{I_D}{I_G}\right)^{-1} \quad (1)$$

Furthermore, photoluminescence (PL) measurement was observed and were measured on a JASCO FP-8600 Spectrophotometer under room temperature utilizing a Xenon arc lamp as the excitation source. The excitation energy was 281 nm with a scanning speed of 1000 nm/min.

2.2.3. XRD analysis

The biochar sample's structure was investigated using an XRD diffractometer (Malvern PANalytical system model Empyrean) that had been configured to run at 40 kV and 40 mA and fitted with a standard Cu–K radiator. A copper target of the radiator is utilized to produce Cu Kα1 8.04 keV X-ray at room temperature. By employing the Bragg-Brentano geometry diffraction method, XRD measurements were achieved for 2 theta values ranging from 5 to 80 at a scanning step time of 148 s and a step size of 0.026. We used the strongest diffraction peak, which was seen near $2\theta \approx 29.5^{\circ}$, 36.9, 39.5, to figure out the size of the crystallites, the lattice strain, and the dislocation density. Without making any adjustments for instrumental broadening, the full width at half maximum (β) was taken directly from the observed peak. So, the values that were calculated are seen as relative estimates that can be used to compare changes in structure caused by electron irradiation. The following formulas were employed to calculate the structural parameters including crystallite size (D) (equation (2)) (Seehra & Pavlovic, 1993), micro strain (ε) (equation (3)) (Bindu & Thomas, 2014), and dislocation density (δ) (equation (4)) (Islam et al., 2024).

$$Crystallite\ size, D = \frac{k\lambda}{\beta \cos\theta} \tag{2}$$

$$Micro\ starin, \in = \frac{\beta}{4 \tan\theta} \tag{3}$$

$$Dislocation\ density, \delta = \frac{1}{D^2} \tag{4}$$

in this context, D = Crystallite size, λ = 0.154 nm = X-ray wavelength, θ = Bragg angle, K = 0.94 = Scherrer-constant, and β = Appropriate Bragg line FWHM on regular 2θ scans.

3. Results

3.1. Morphological analysis by SEM/EDX

Radiation-induced surface damage has been observed, and the corresponding distribution of the incorporating elemental content of the samples has been ascertained by employing SEM-EDX analysis. The biochar sample has an elevated level of carbon (94.22 %). The additional components include calcium (Ca 0.45 %), potassium (K) (1.63 %), and oxygen (3.70 %). The number of luminescence and trapping centers in biochar is believed to be considerably increased by the presence of these impurities (Nawi et al., 2020), thereby inadvertently improves the TL response of this media. Images from the SEM of promising biochar samples exposed to varied radiation doses are displayed in Fig. 1. In contrast to 4 Gy, microstructural-damage is distinctly observable at 10 Gy and 20 Gy. The mean particle size of the biochar samples irradiated at 4 Gy, 10 Gy, and 20 Gy was analyzed from two-dimensional SEM micrographs using ImageJ software (Thilagashanthi et al., 2021). This analysis was based on the projected shape of the particles in the 2D images and represents a one-dimensional approximation of particle length for randomly selected 15 particles, focusing on particles with clearly visible boundaries within a specific portion of the SEM images. The observed average particle lengths for 4 Gy, 10 Gy, and 20 Gy were 70.0 ± 0.46 μm, 60.0 ± 0.36 μm, and 58.0 ± 0.47 μm, respectively. This demonstrates that the particles size became smaller as the radiation dose became higher. The standard deviation shows that particle fragmentation and agglomeration are naturally uneven, which is common for carbon materials made from pyrolyzed biomass (Tripathi et al., 2016; Tan et al., 2015). The variety of particle sizes may also affect the surface area, the distribution of defects, and interaction behavior of the material with exposed radiation. The reduction of particle size is attributed to radiation-induced structural damage, where ionizing radiation disrupts atomic bonds, causing fractures and particle fragmentation. This study focuses on the mean particle length and SEM images for comparing morphological changes across irradiation doses, we acknowledge that a full particle size distribution analysis would offer deeper insight and plan to address this in future work. Additionally, the SEM images revealed an increase in porosity with higher doses, as indicated by the presence of hollow and expanded pore structures. This increased porosity can be explained by radiation-induced defects and localized material disintegration within the carbon matrix. Although variations in SEM focus across images may affect the absolute values of particle size, the observed trend remains consistent. These findings highlight the influence of irradiation on the microstructure of biochar, with potential implications for its dosimetric applications.

3.2. Raman spectroscopy analysis

Through the examination of defect states, this exploratory study assessed the efficacy of utilizing Raman spectroscopy to identify radiation driven damage in biochar subjected to electron irradiation doses between 0 and 20 Gy. The detection of defects in carbonaceous materials

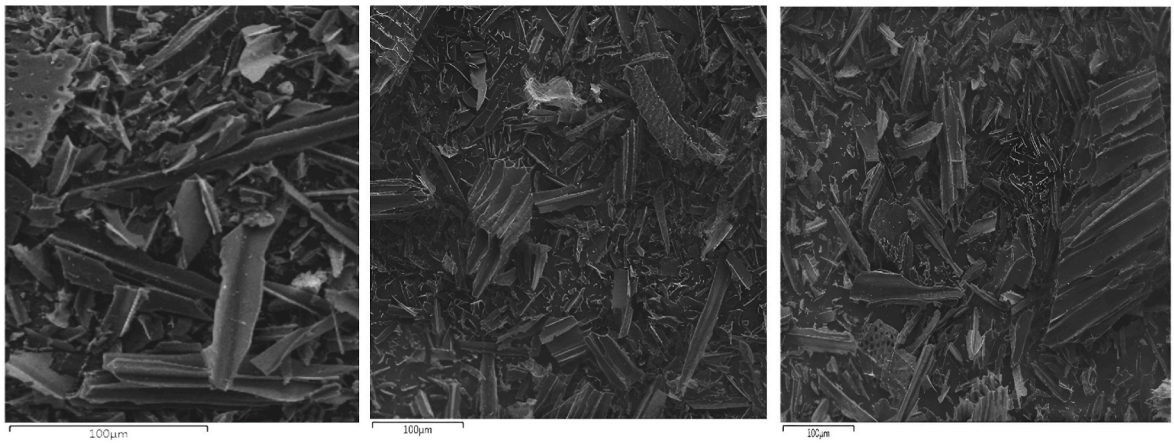

Fig. 1. SEM images of biochar sample (a) at 4 Gy (b) 10 Gy and (c) 20 Gy.

is typically accomplished by the utilization of the integrated ratio of intensity (I_D/I_G) of the D and G bands (Elcey & Manoj, 2016). As anticipated for high-purity carbon, the sample revealed two distinct bands with a fewer number of defects in the D band around 1353 cm^{-1} (see Fig. 2(a)). The D band originates for the breathing vibration of the in-plane aromatic ring structure, whereas the G band is caused for the stretching vibration of the sp^2 carbon or the in-plane stretching of the hexagonal carbon rings. The wide peak of the second-order zone, which extends approximately 2200 to near 3500 cm^{-1}, is comparable to the findings of human hair (Lam et al., 2021). While the D + G band, which is seen at about 2900 cm^{-1}, is associated with second-order Raman scattering from the samples, the G′ or 2D band is regarded as the overtone of the D band at around 2700 cm^{-1} (see Fig. 2(a)). Fig. 2 (b) depicts the dose dependent variation for electron irradiated biochar. Biochar exhibits highly porous and amorphous nature. Biochar possesses C (94.22 %), and impurities (5.78 %). Impurities like K, Ca, and O found in biochar are thought to affect the quantity of trapping or luminescence centers in carbonaceous material (Mat Nawi et al., 2022). Oxygen is also thought to be a source for luminescence centers, and the variations in trapping centers are thought to be the cause of the sensitivity variations seen in samples exposed to varying radiation doses. The correlation between the crystallite size (L_a) and I_D/I_G ratio has been studied in order to determine the extent of radiation driven damage to the carbonaceous samples using the generalized Tuinstra-Koenig equation. An inverse relationship between L_a and I_D/I_G for the examined samples is plotted in Fig. 3(a), suggesting a higher defect density with smaller crystallite size inside the biochar's amorphous microstructure. Additionally, the results presented here are consistent with (Bradley et al., 2021). The I_D/I_G ratio clearly shows the defect density in porous biochar. As a consequence of radiation-induced internal annealing, Fig. 3(b) also illustrates the progression of radiation driven damage in a cyclical way that suggests competition between the formation and reduction of defects. This phenomenon has been identified and reported in previous graphite-based studies by (Bradley et al., 2019; Bradley et al., 2021; Sani et al., 2020), and (Nawi et al., 2020, 2021) as well as the study on human hair performed by (Lam et al., 2021). The value of I_D/I_G at different doses are listed in Table 1. Fig. 4 (a) demonstrates the deconvolution of first order peaks for Raman spectra of electron irradiated biochar with several peaks and their center located between 1199 and 1586.99 cm^{-1} (see Fig. 4(a)). This range is attributed to the C–C and C=C stretching vibration modes of amorphous carbon and polyene-like structure (Mat Nawi et al., 2022). Fig. 4(b) demonstrates the deconvolution of high frequency regions of the Raman spectra. These deconvoluted peaks are located in the range of 2200–3400 cm^{-1}. Furthermore, the area under each deconvoluted curve of the first and second order regions of the Raman spectra was additionally employed to investigate the effects of electron irradiation on the biochar sample. This method was implemented from (Khandaker et al., 2022). A cyclic pattern that is dose dependent and similar to that of (Khandaker et al., 2022) and (Muslima et al., 2024a) is revealed in Fig. 4(c) and (d). It indicates the development of defects as well as the energy that has been stored for allowing the full or partial internal annealing of structural changes.

3.3. Photoluminescence (PL) analysis

With a carbon concentration of nearly 94 %, biochar samples reveal separate two PL peaks, that centred at roughly 281 nm and 339 nm, corresponding to the first and second peak of the PL spectrum. The PL spectra for different doses is depicted in Fig. 5(a). The emission peak intensity, emission peak area and full-width at half maxima (FWHM) were plotted against the delivered dose and depicted in Fig. 5(b)–(c) and (d) respectively. The data indicates an oscillatory pattern that suggests a competition between defect generation and irradiation-driven annealing of defects. Radiation-driven suppression mechanisms including cross-linking and defect creation are thought to produce fluctuations in the intensity and area of the emission spectra, which causes retrapping over the dose range. The average value for the band gap energy (E_g) of the irradiated samples has been assessed using the following relation (equation (5)):

$$\textit{Mean bandgap energy}, E_g = \frac{hc}{\lambda} \tag{5}$$

where h = Planck constant, c = Speed of light and λ = Wavelength of the peak location of the emission spectra.

Photoluminescence measurements were performed using a 281 nm excitation laser, and the emission peak was observed at approximately 339 nm. The band gap energy for the pre-irradiated investigated samples has been calculated to be 4.63 ± 0.01 eV, suggesting a comparatively broad band gap. In thermoluminescent dosimetry, a wide band gap is advantageous as it facilitates the creation of deep and stable trapping centers for charge carriers induced by radiation. This enhances signal retention and thermal resistance, especially under post-irradiation storage conditions (Chen & McKeever, 1997; McKeever, 1985). Prior studies conducted by Muslima et al., 2025 (Muslima et al., 2024); have shown that biochar maintains its integrity with minimal fading over prolonged storage durations, reinforcing the claim that the deeper traps linked to a larger band gap are proficient in safeguarding the stored luminescent signal. The enhanced reliability and stability of dose measurements over time can be attributed to biochar's higher band gap, suggesting less chance of thermal release in comparison to traditional TL materials such as LiF:Mg,Ti, which possess a band gap of approximately 3.3 eV (Chen & McKeever, 1997).

3.4. XRD analysis

X-ray diffraction (XRD) has been performed to evaluate the effect of radiation on the biochar sample. At room temperature, the XRD pattern 2θ ranged between 5° and 80° with a scanning step length of 148 s and

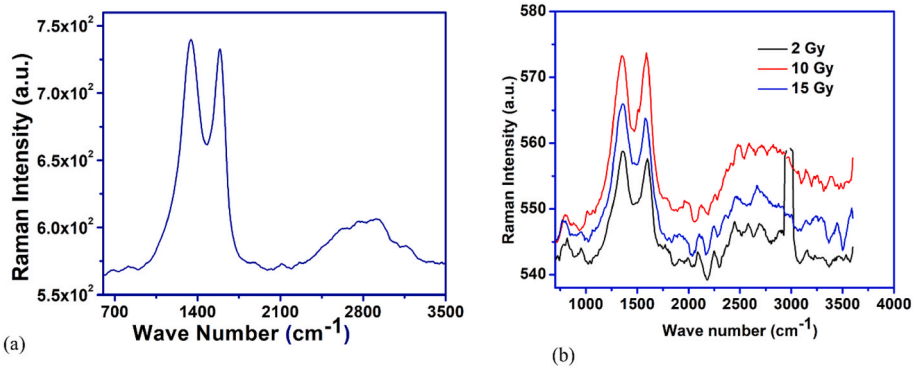

Fig. 2. Raman spectrum for (a) non irradiated and (b) irradiated samples at different doses.

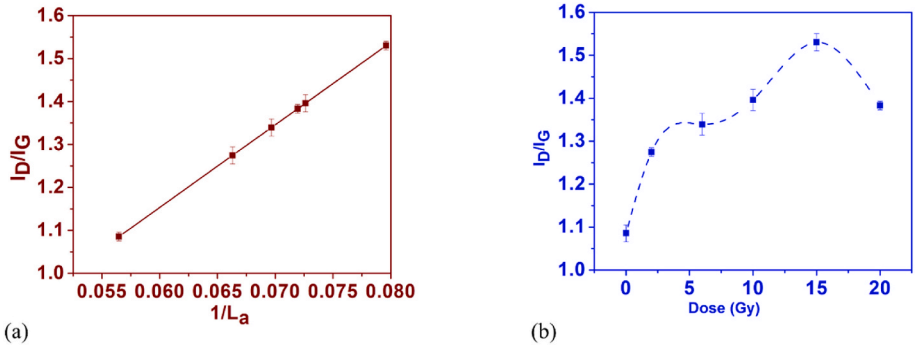

Fig. 3. Graph between (a) $1/L_a$ vs I_D/I_G (b) Dose vs I_D/I_G for electron irradiation doses ranges within 0–20 Gy. (Note that error bar is smaller than the data point).

Table 1
Evolution of I_D/I_G at different doses for electron irradiation.

No. of Observations	Doses (Gy)	ID/IG
1	0	1.08 ± 0.02
2	2	1.27 ± 0.01
3	6	1.33 ± 0.025
4	10	1.39 ± 0.025
5	15	1.53 ± 0.02
6	20	1.38 ± 0.01

dose ranging between 0 and 20 Gy. The molecular microstructure of biochar can be affected by electron irradiation, which may modify the crystallite size. In our prior study, Muslima et al., 2025 used XRD to characterize the structure of biochar at photon doses ranging between 2 and 20 Gy and demonstrated a broad range 2θ peak between 18° and 28°, which indicates the disordered graphite structure, suggesting that biochar sample has an amorphous like carbon structure with a plane index of (002), and this can be attributed to the combination of amorphous and nanocrystalline phases (Xing et al., 2013). Pies et al. (2008) conducted an independent investigation and identified a similar XRD pattern for wood-based Japanese Cedar charcoal carbonized material. In the present study, structural information including the size of the crystallite, density of dislocation, micro-strain, and full-width at half-maxima (FWHM) for 6 MeV electron irradiation dose ranging between 2 and 20 Gy are investigated for the biochar sample from XRD pattern, and the results are listed in Table 2. Table 2 presents the dose dependent variation in the structural parameters which supports the morphological analysis. Table 2 shows that the crystallite size from the peak of 29.5° and 36.9° is decreasing with the increasing radiation dose, while the defect density is increasing with decreasing crystallite size. This is also confirmed by the raman spectroscopy analysis (see Fig. 3(a)). High defect density arises in the situation of decreased crystallite size because the crystallite structure is more disordered close to grain boundaries, where a greater proportion of atoms are found in smaller crystallites. The total defect density rises as a result of grain boundaries. Furthermore, the crystallite size for peak position 39.5° firstly increases and then once again decreases. The dislocation density for this peak position is also decreasing with increasing crystallite size. This may be arisen for the fluctuation of peak position (see Fig. 6(d)). The reason behind this has been discussed later in this section. It's important to note that Scherrer's equation isn't always the best way to figure out crystallites size. This is especially true for materials like biochar that have broad diffraction peaks and a mix of amorphous and nanocrystalline

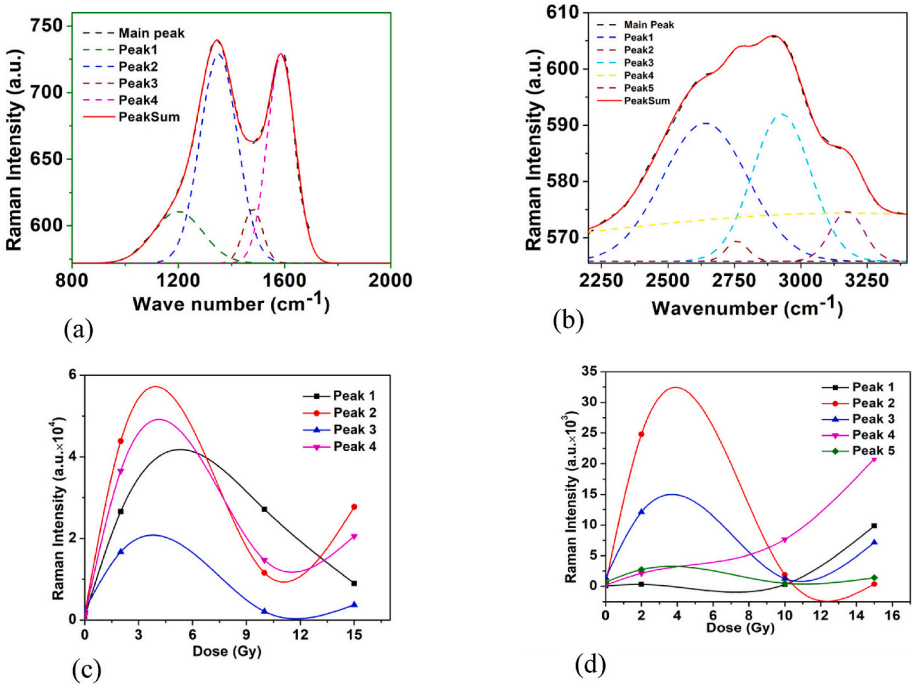

Fig. 4. (a) Deconvoluted 1st order peaks of Raman spectra (b) Deconvoluted high frequency region of Raman spectra (c) Dose dependent deconvoluted peak area of 1st order peak (d) Dose dependent deconvoluted peak area of high frequency region.

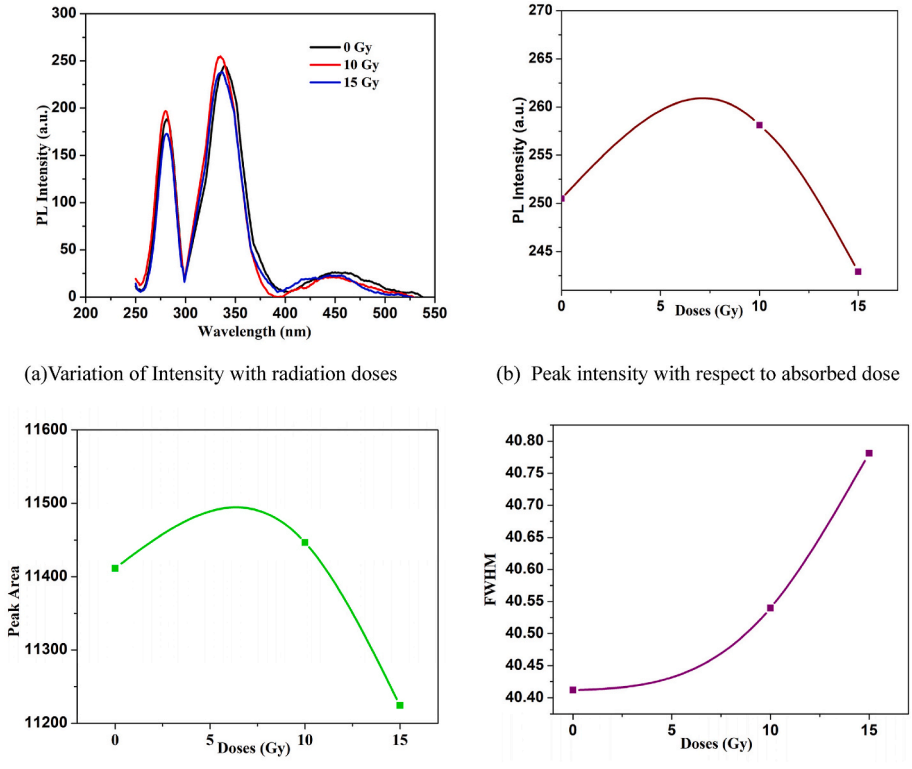

(a)Variation of Intensity with radiation doses

(b) Peak intensity with respect to absorbed dose

(c) Peak area with respect to dose

(d) Variation of FWHM with doses

Fig. 5. PL spectra analysis with respect to radiation doses for 6 MeV electron irradiation. Note that the error bars are smaller than each data points.

Table 2
Summarized information on dose dependent changes of structural parameters obtained from XRD pattern.

Doses (Gy)	Peak position 2-theta	Atomic spacing, d	Full-width at half-maxima (FWHM)	Size of the crystallite, D (nm)	Area of the peak	Intensity (a. u.)	Density of Dislocation, δ $\times 10^{-4}$	Lattice strain, ε
2	29.5	0.30	0.88	9.66 ± 0.015	3675.09	4498.82	106.96 ± 0.015	0.84 ± 0.015
	36.9	0.24	0.80	10.87 ± 0.02	1759.96	3347.11	84.51 ± 0.02	0.60 ± 0.02
	39.5	0.22	1.18	7.46 ± 0.025	2809.92	3207.96	179.37 ± 0.025	0.82 ± 0.025
10	29.5	0.30	0.98	8.65 ± 0.01	4193.06	4994.39	133.61 ± 0.01	0.93 ± 0.01
	35.87	0.22	0.85	10.19 ± 0.025	1798.48	3234.42	96.24 ± 0.025	0.66 ± 0.025
	39.9	0.22	0.96	9.12 ± 0.02	1829.73	3128.78	120.19 ± 0.02	0.66 ± 0.02
20	29.5	0.30	1.01	8.42 ± 0.01	4808.14	5160.95	140.74 ± 0.01	0.96 ± 0.01
	35.8	0.25	0.89	9.7 ± 0.015	1963.81	3670.23	105.43 ± 0.015	0.69 ± 0.015
	39.5	0.22	1.40	6.29 ± 0.025	1974.97	3448.50	252.48 ± 0.025	0.97 ± 0.02

domains. In these kinds of systems, peaks can get wider not just because the crystallites are small, but also because of lattice strain, structural disorder, and the presence of turbostratic carbon. They are mostly used as relative indicators to keep track of how structures change when they are exposed to radiation, not as absolute measurements of the sizes of crystalline domains."Full Proof software" is also employed to refine and analyze the XRD pattern by employing Rietveld Refinement (Birajdar et al., 2022). The Rietveld refinement of the XRD pattern of the nonir-radiated sample is displayed in Fig. 6 (a). The refinement has an acceptable Chi^2 of 1.7232. The Rietveld Refinement confirms the amorphous carbon structure with an exact plane index of (002). Fig. 6(b) depicts the XRD refinement revealed a C-C bonded structure that was obtained from the biochar sample's XRD refinement outputs. A more comprehensive understanding of the physicochemical behavior of bio-char can be rendered possible by the revealed structure, which offers insights into its crystallographic characteristics. Fig. 6(c) shows the XRD pattern comparison for 6 MeV electron dose from 0 to 20 Gy. Radiation-induced alterations or radiation impacts on material structure can be better understood by using this comparison. As the dose increases, the intensity and structural parameters vary to some extent, and the peak at $2\theta = 39.5^{\circ}$ shifts its position, as shown in Table 2 and Fig. 6(c) and (d). The biochar samples exhibit comparable fluctuating patterns within the dose range under investigation, which supports the Raman analysis earlier presented in this study. Bradley et al. (2022) provided an in-depth explanation of this scenario. Carbonaceous mate-rial possesses an obsessive capacity to self-heal, absorbing damage that might otherwise result in dissipation and distortion. In this regard, an increase in irradiation dose results in a corresponding rise in the number of electrons produced through the Compton effect (Sani et al., 2020). Carbon atoms may be displaced by these electrons through forceful ("knock-on") collisions, and a collision cascade may also happen if the colliding electrons' energies are greater than the material's threshold displacement energy (Almugren et al., 2022). The rearrangements of carbon atoms from their lattice location are typically thought to break the C-C bonds, resulting in Frenkel defects and dangling bonds (immo-bilized free radicals), which raises the material's structural disorder. However, carbon-based material has a self-repairing mechanism that makes it possible to avoid defects at higher energy like vacancies and

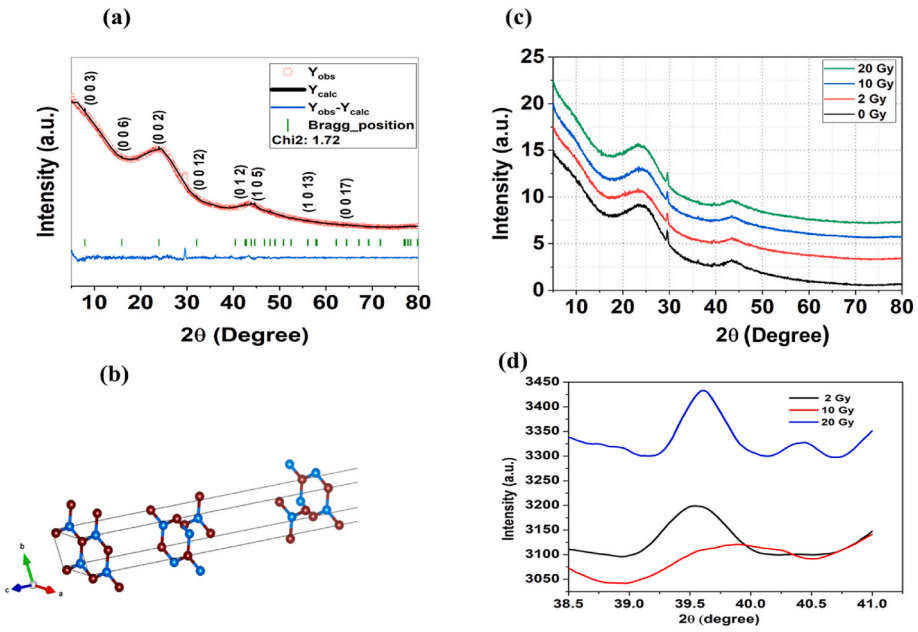

Fig. 6. (a) Rietveld refinement of the XRD pattern for nonirradiated biochar sample (b) Crystal structure of a C-C bonded arrangement (c) XRD pattern comparison for 6 MeV electron at 0–20 Gy (d) Focusing on the peak at position 39.5° for biochar at 2, 10, 20 Gy of 6 MeV electron irradiation.

holes, as noted by (Bradley et al., 2020; Ding et al., 2007). Hence, by the saturation of dangling bond and developing rings of non-hexagonal, the radiation-induced vacancies can be compensated (Li et al., 2013). Moreover, Telling et al. (2003) postulated that complex formation over the wide inter-layer distance could stabilize vacancy defects in carbonaceous material.

4. Conclusion

The microstructure and structural alteration of commercial coconut shell biochar have been investigated in the current study, which uses electron-mediated interactions at radiotherapy dose range as a fine medium for application in radiation dosimetry. To study the change in morphological and structural characteristics of the carbon-based samples, biochar was examined using SEM, Raman spectroscopy, PL and XRD techniques. The results for SEM, Raman spectroscopy, PL and XRD are observed to be supportive to one another, and their microscopic responses to irradiation doses well explained the situation. Microstructural damage is clearly observable by SEM with the increasing dose of electron irradiation and notable structural alterations were discovered at the specified doses, as seen by variations in the shape and intensity of raman spectra. For irradiated samples with dose ranging between 2 and 20 Gy, the cyclical patterns of peak areas from raman deconvoluted peaks and intensity ratios (I_D/I_G) imply notable structural changes and internal defect annealing. The peak area and FWHM of PL analysis also confirms the dose dependent structural alteration of biochar. Additionally, the structural parameters obtained from XRD pattern also support these phenomena. These structural alterations introduce defects, can create localized states of energy within the band gap, which have a direct influence on charge carrier trapping and recombination processes. These defect-created states can increase luminescence and modify peak intensity. In addition, crystallite size variations as observed in XRD, influence electronic structure and trap depth distribution, thereby influencing thermoluminescence (TL) properties. Therefore, the structural analysis confirms that the biochar offers good potential to be used in electron dose measurements for radiotherapy application, however, there are some limitations such as this study did not validate the TL readout. Future research should look into the thermoluminescent behavior of irradiated biochar to observe the dose-response and linearity. Also, the long-term stability and fading behavior of the material's radiation response still need to be carefully studied. These issues need to address to confirm biochar as a reliable and potential choice for radiation dosimetry.

CRediT authorship contribution statement

Umme Muslima: Writing – original draft, Methodology, Investigation, Formal analysis, Data curation, Writing – review & editing. **MayeenUddin Khandaker:** Writing – review & editing, Supervision, Methodology, Conceptualization. **S.N. Mat Nawi:** Writing – review & editing, Methodology, Investigation. **MdRaghib Rahat:** Writing – original draft, Methodology, Investigation. **S.E. Lam:** Writing – review & editing, Supervision, Methodology. **H.J. Woo:** Writing – review & editing, Visualization, Resources, Methodology. **N.M. Ung:** Writing – review & editing, Software, Resources, Methodology. **Nora Almuqbil:** Writing – review & editing, Software, Resources, Project administration, Funding acquisition. **Zuhal Y. Hamd:** Writing – review & editing, Software, Resources, Project administration, Funding acquisition. **Chien Ing Yeo:** Writing – review & editing, Software, Resources, Methodology.

Availability of data and materials

All data are available in the manuscript.

Declaration of generative AI and AI-assisted technologies in the writing process

During the preparation of this work the author(s) used some online service/tools such as Grammarly, ChatGPT 4.0 in order to improve language and readability. After using this tool/service, we reviewed and edited the content as needed and take(s) full responsibility for the content of the publication.

Funding

This work was funded by Princess Nourah bint Abdulrahman University Researchers Supporting Project number (PNURSP2025R850), Princess Nourah bint Abdulrahman University, Riyadh, Saudi Arabia.

Competing interests

The authors declare that they have no known competing financial interests or personal relationships that could have appeared to influence the work reported in this paper.

Acknowledgment

The authors extend their appreciation to Princess Nourah bint Abdulrahman University Researchers Supporting Project number (PNURSP2025R850), Princess Nourah bint Abdulrahman University, Riyadh, Saudi Arabia.

References

Ajien, A., Idris, J., Md Sofwan, N., Husen, R., & Seli, H. (2023). Coconut shell and husk biochar: A review of production and activation technology, economic, financial aspect and application. *Waste Management & Research, 41*(1), 37–51.

Almugren, K., Sani, S. A., Sulong, I. A., Nawi, S. M., Shafiqah, A. S., & Bradley, D. (2022). Structural and defect changes in black carbon charcoal irradiated with gamma ray. *Radiation Physics and Chemistry, 200*, Article 110331.

Bindu, P., & Thomas, S. (2014). Estimation of lattice strain in ZnO nanoparticles: X-Ray peak profile analysis. *Journal of Theoretical and Applied Physics, 8*, 123–134.

Birajdar, S. D., Saraf, A. R., Maharolkar, A. P., Gattu, K. P., Patil, N. G., Chavan, R. B., Jamkar, M. V., Mundhe, Y. S., Kambale, R. N., & Alange, R. C. (2022). Intrinsic defect-induced magnetism and enhanced photocatalytic activity in Zn1− xZrxO (0.0≤ x≤ 0.07) nanoparticles for spintronic device and photocatalytic application. *Journal of Alloys and Compounds, 929*, Article 167272.

Bradley, D. A., Ee, L. S., Mat Nawi, S. N., Abdul Sani, S. F., Khandaker, M., Alzimami, K., & Jambi, L. (2021). Graphite sheets in study of radiation dosimetry and associated investigations of damage. *Applied Radiation and Isotopes, 174*, Article 109769. https://doi.org/10.1016/j.apradiso.2021.109769

Bradley, D., Ee, L. S., Nawi, S. N. M., Sani, S. F. A., Khandaker, M., Alzimami, K., Jambi, L., & Alqhatani, A. (2022). Radiation induced defects in graphite. *Applied Radiation and Isotopes, 182*, Article 110141.

Bradley, D., Nawi, S. N. M., Khandaker, M. U., Almugren, K., & Sani, S. A. (2020). Sub kGy photon irradiation alterations in graphite. *Applied Radiation and Isotopes, 161*, Article 109168.

Bradley, D., Rozaila, Z. S., Khandaker, M., Almugren, K., Meevasana, W., & Sani, S. A. (2019). Raman spectroscopy and X-ray photo-spectroscopy analysis of graphite media irradiated at low doses. *Applied Radiation and Isotopes, 147*, 105–112.

Brooks, J. K., Bashirelahi, N., & Reynolds, M. A. (2017). Charcoal and charcoal-based dentifrices: A literature review. *The Journal of the American Dental Association, 148*(9), 661–670.

Chen, R., & McKeever, S. W. (1997). *Theory of thermoluminescence and related phenomena. World Scientific Publishing Co. Pte. Ltd* (p. 576). https://doi.org/10.1142/2781. #9789812830890.

Ding, F., Jiao, K., Lin, Y., & Yakobson, B. I. (2007). How evaporating carbon nanotubes retain their perfection? *Nano Letters, 7*(3), 681–684.

Elcey, C., & Manoj, B. (2016). Graphitization of coal by bio-solubilization: Structure probe by Raman spectroscopy. *Asian Journal of Chemistry, 28*(7), 1557.

Ighalo, J. O., Conradie, J., Ohoro, C. R., Amaku, J. F., Oyedotun, K. O., Maxakato, N. W., … Adegoke, K. A. (2023). Biochar from coconut residues: An overview of production, properties, and applications. *Industrial Crops and Products, 204*, Article 117300.

Islam, S. A., Kamruzzaman, M., Rahat, M. R., Hossain, S., Abdul-Rashid, H. A., Khandaker, M. U., Bradley, D. A., Al-Mamun, M., & Rahman, A. K. M. M. (2024). LiZnBO3 phosphor for dosimetry applications. *Radiation Physics and Chemistry, 218*, Article 111596. https://doi.org/10.1016/j.radphyschem.2024.111596

Khan, S.u. D., Arora, M., Wahab, M., & Saini, P. (2014). Permittivity and electromagnetic interference shielding investigations of activated charcoal loaded acrylic coating compositions. *Journal of Polymers, 2014*(1), Article 193058.

Khandaker, M. U., Nawi, S. N. M., Lam, S. E., Bradley, D. A., Sani, S. F. A., Faruque, M. R. I., Yasmin, S., & Idris, A. M. (2022). Studies of defect states and kinetic parameters of car windscreen for thermoluminescence retrospective dosimetry. *Applied Radiation and Isotopes, 186*, Article 110271. https://doi.org/10.1016/j.apradiso.2022.110271

Lam, S., Bradley, D., Nawi, S. M., Khandaker, M., & Sani, S. A. (2023). Carbon rich media for luminescence-based surface dosimetry and study of associated surface defects. *Applied Radiation and Isotopes, 199*, Article 110920.

Lam, S. E., Mat Nawi, S. N., Abdul Sani, S. F., Khandaker, M. U., & Bradley, D. A. (2021). Raman and photoluminescence spectroscopy analysis of gamma irradiated human hair. *Scientific Reports, 11*(1), 7939. https://doi.org/10.1038/s41598-021-86942-4

Li, B., Feng, Y., Ding, K., Qian, G., Zhang, X., & Zhang, J. (2013). The effect of gamma ray irradiation on the structure of graphite and multi-walled carbon nanotubes. *Carbon, 60*, 186–192.

Li, C., Wang, D., & Kong, L. (2021). Application of machine learning techniques in mineral classification for scanning electron microscopy-energy dispersive X-ray spectroscopy (SEM-EDS) images. *Journal of Petroleum Science and Engineering, 200*, Article 108178.

Mat Nawi, S. N., Khandaker, M. U., Sani, S. F. A., Lam, S. E., Ung, N. M., Almugren, K. S., & Bradley, D. A. (2022). Low-cost commercial graphite-rich pencils subjected to electron irradiation for passive radiation dosimetry. *Applied Radiation and Isotopes, 188*, Article 110419. https://doi.org/10.1016/j.apradiso.2022.110419

McKeever, S. W. (1985). *Thermoluminescence of solids* (Vol. 3). Cambridge university press.

Muslima, U., Khandaker, M. U., Nawi, S. N. M., Lam, S. E., Sani, S. F. A., Bradley, D. A., Mahmoud, M., & Woo, H. J. (2024). Thermoluminescence characterization of biochar material for dosimetric applications. *Nuclear Engineering and Technology*. , Article 103348. https://doi.org/10.1016/j.net.2024.103348

Muslima, U., Khandaker, M. U., Lam, S. E., Nawi, S. N. M., Sani, S. F. A., Bradley, D. A., Ung, N. M., Mahmoud, M., Saidur, R., & Woo, H. J. (2025). Thermoluminescence and structural characterization of biochar in the photon doses of 2–20 Gy for dosimetric applications. *Radiation Physics and Chemistry, 227*, Article 112386. https://doi.org/10.1016/j.radphyschem.2024.112386

Muslima, U., Khandaker, M. U., Nawi, S. N. M., Lam, S. E., Sani, S. F. A., Bradley, D. A., Saidur, R., Tan, Y. S., Osman, H., Hanfi, M. Y., & Issa, S. A. M. (2024a). Investigation of structural and TL kinetic parameters of smartphone screen protector glasses for applications in retrospective dosimetry. *Radiation Physics and Chemistry, 224*, Article 112093. https://doi.org/10.1016/j.radphyschem.2024.112093

Nawi, S. N. M., Khandaker, M. U., Bradley, D., Sani, S. A., Almugren, K., & Sulieman, A. (2020). Polymer pencil lead graphite for in vivo radiation dosimetry. *Diamond and Related Materials, 106*, Article 107860.

Nawi, S. M., Khandaker, M. U., Sani, S. A., Ung, N., Lam, S., Al-mugren, K., & Bradley, D. (2021). The potential of polymer pencil-lead graphite for clinical electron beam dosimetry. *Nuclear Instruments and Methods in Physics Research Section A: Accelerators, Spectrometers, Detectors and Associated Equipment, 1010*, Article 165478.

Pies, C., Hoffmann, B., Petrowsky, J., Yang, Y., Ternes, T. A., & Hofmann, T. (2008). Characterization and source identification of polycyclic aromatic hydrocarbons (PAHs) in river bank soils. *Chemosphere, 72*(10), 1594–1601.

Sani, S. A., Ismail, S., Almugren, K., Khandaker, M. U., & Bradley, D. (2020). Dosimetric utility of structural changes in gamma irradiated graphite-rich pencils. *Radiation Physics and Chemistry, 171*, Article 108703.

Seehra, M. S., & Pavlovic, A. S. (1993). X-Ray diffraction, thermal expansion, electrical conductivity, and optical microscopy studies of coal-based graphites. *Carbon, 31*(4), 557–564. https://doi.org/10.1016/0008-6223(93)90109-N

Tan, X., Liu, Y., Zeng, G., Wang, X., Hu, X., Gu, Y., & Yang, Z. (2015). Application of biochar for the removal of pollutants from aqueous solutions. *Chemosphere, 125*, 70–85.

Telling, R. H., Ewels, C. P., El-Barbary, A. A., & Heggie, M. I. (2003). Wigner defects bridge the graphite gap. *Nature Materials, 2*(5), 333–337.

Thilagashanthi, T., Gunasekaran, K., & Satyanarayanan, K. (2021). Microstructural pore analysis using SEM and ImageJ on the absorption of treated coconut shell aggregate. *Journal of Cleaner Production, 324*, Article 129217.

Tripathi, M., Sahu, J. N., & Ganesan, P. (2016). Effect of process parameters on production of biochar from biomass waste through pyrolysis: A review. *Renewable and Sustainable Energy Reviews, 55*, 467–481.

Tuinstra, F., & Koenig, J. L. (1970). Raman spectrum of graphite. *The Journal of Chemical Physics, 53*(3), 1126–1130.

Xing, T., Li, L. H., Hou, L., Hu, X., Zhou, S., Peter, R., Petravic, M., & Chen, Y. (2013). Disorder in ball-milled graphite revealed by Raman spectroscopy. *Carbon, 57*, 515–519.